ADVANCED MATERIALS
www.advmat.de

Perovskite Wide-Angle Field-Of-View Camera

Zhong Ji, Yujin Liu, Chuanxi Zhao, Zhong Lin Wang, and Wenjie Mai**

Researchers have attempted to create wide-angle field-of-view (FOV) cameras inspired by the structure of the eyes of animals, including fisheye and compound eye cameras. However, realizing wide-angle FOV cameras simultaneously exhibiting low distortion and high spatial resolution remains a significant challenge. In this study, a novel wide-angle FOV camera is developed by combining a single large-area flexible perovskite photodetector (FP-PD) using computational technology. With this camera, the proposed single-photodetector imaging technique can obtain high-spatial-resolution images using only a single detector, and the large-area FP-PD can be bent further to collect light from a wide-angle FOV. The proposed camera demonstrates remarkable features of an extraordinarily tunable wide FOV (greater than 150°), high spatial resolution of 256 × 256 pixels, and low distortion. It is believed that the proposed compatible and extensible camera prototype will promote the development of high-performance versatile FOV cameras.

1. Introduction

Wide-angle field-of-view (FOV) imaging is a goal that people always pursue as it can provide a delightful panoramic picture of the landscape. Wide-FOV imaging can assist in automatic driving (a typical application of artificial intelligence) and can be used to create a hypothetical 3D visual world (virtual reality). Limited by the physical distribution of visual cells, human eyes have a very narrow (≈60°) high-quality FOV (direct sight) accompanied by a wider (single eye: ≈155°) low-quality FOV (peripheral vision).[1] To be specific, before being perceived by the retina, lights go through a series of refractive structures, including the cornea, crystalline lens, and vitreous body, as shown in **Figure 1**a. Paraxial rays can reach the center of the retina, which is full of cone cells (in charge of color vision), forming a high-quality FOV. Owing to refraction, off-axis rays can only reach the margin of the retina, forming a low-quality FOV. However, very large-angle off-axis rays cannot reach the retina and form an invisible region. The composition of cameras is very similar to that of the human eye; that is, camera lenses are equivalent to the refractive structures mentioned above, and a negative plate or charge coupled device (CCD) is equivalent to the retina. In contrast, photoreceptors in the negative plate or CCD are uniformly distributed, resulting in a consistent resolution in the images. Furthermore, researchers have attempted to fabricate artificial electronic eyes to achieve a wider FOV, lower aberrations, and less optical component imaging.[2–4] However, because of the complicated manufacturing process of hemispherical artificial electronic eyes, it is difficult to realize high-density detector arrays in the hemisphere. Therefore, it is still a huge challenge to realize wide-FOV artificial electronic eyes with high resolution.

In the case of limited FOV of photosensitive systems, there are still some strategies to realize wide-angle FOV imaging such as staying away from the imaging object. Quantitatively, to view the entire scene, the camera should satisfy the condition that the scene angle (θ) is less than the FOV of the cameras (α_F), as shown in Figure 1b. According to the geometrical relation, $\tan(\theta/2) = L/D$, where L denotes the projection width of the scene and D is the distance between the scene and camera; increasing the distance (D) is beneficial for viewing the entire scene. Another possible approach is stitching images from different angles into one wide-angle image, which is referred to as image mosaic.[5] However, the above strategies limit the application scopes.

The fundamental solution to this problem is to improve the FOV of the camera (α_F). In recent years, researchers have been inspired by nature to develop cameras such as fisheye cameras, which have a fish-eyeball-like hemispherical appearance and can achieve a wider FOV (up to 230°) than human eyes.[6] However, this inevitably results in optical aberration, particularly for barrel-shaped distortion because of the collection of

Z. Ji, Y. Liu, C. Zhao, W. Mai
Siyuan Laboratory
Guangdong Provincial Engineering Technology Research
Center of Vacuum Coating Technologies and New Energy Materials
Department of Physics
Jinan University
Guangzhou, Guangdong 510632, China
E-mail: wenjiemai@email.jnu.edu.cn
Z. Ji
Guangzhou Institute of Technology
Xidian University
Guangzhou, Guangdong 510555, China
Z. L. Wang, W. Mai
CAS Center for Excellence in Nanoscience
Beijing Key Laboratory of Micro-Nano Energy and Sensor
Beijing Institute of Nanoenergy and Nanosystems
Chinese Academy of Sciences
Beijing 100083, China
E-mail: zhong.wang@mse.gatech.edu
Z. L. Wang
School of Materials Science and Engineering
Georgia Institute of Technology
Atlanta, GA 30332, USA
The ORCID identification number(s) for the author(s) of this article can be found under https://doi.org/10.1002/adma.202206957.

DOI: 10.1002/adma.202206957

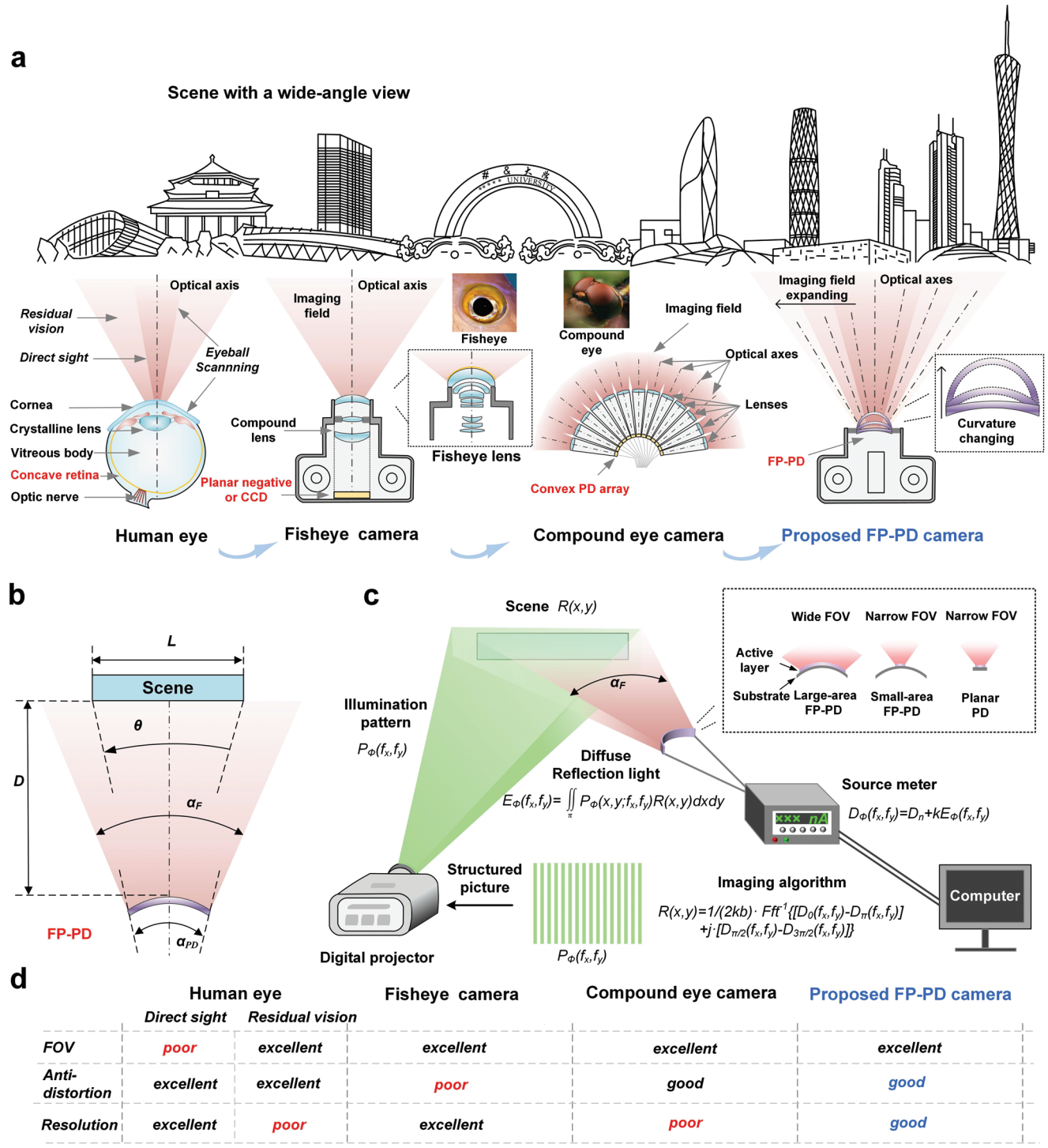

d

	Human eye		Fisheye camera	Compound eye camera	Proposed FP-PD camera
	Direct sight	Residual vision			
FOV	poor	excellent	excellent	excellent	excellent
Anti-distortion	excellent	excellent	poor	good	good
Resolution	excellent	poor	excellent	poor	good

Figure 1. Schematic of a new concept of the FP-PD camera. a) Structure of three types of cameras (fisheye, compound eye, and the proposed FP-PD cameras) for realizing wide-angle FOV as well as human eyes. b) Definitions of parameters regarding scene angle (θ), scene width (L), FOV of cameras (α_F), bending angle of the FP-PD (α_{PD}), and distance (D) in wide-angle FOV imaging. c) Structure of the FP-PD camera prototype. Inserts: schematic of FOV of large-area FP-PD, small-area of FP-PD, and planar PD. d) Comparison of these cameras and human eyes from three aspects (FOV, anti-image distortion, and resolution).

large-angle off-axis light. To reduce aberration, a battery of spherical lenses and technically complex aspheric lenses should be used. However, the barrel-shaped distortion problem has not yet been adequately addressed. For compound eyes of insects (Figure 1a), each ommatidium has its own optical axis, and the entire compound eye has a convex hemispherical appearance.[7] In this condition, lights at different angles can find their nearly paralleled optical axis. Therefore, compound eye cameras

are expected to achieve wide-angle FOV imaging without any barrel-shaped distortions. Some researchers have attempted to fabricate artificial compound eyes and have demonstrated excellent imaging demonstrations.[8–11] However, artificial compound eyes face several challenges. Because each ommatidium has its own optical system, the linearly increasing number of ommatidia increases the fabrication difficulty. In fact, a typical artificial compound eye contains only 180 ommatidia,[11] which is significantly less than the megapixels of conventional digital cameras, leading to an extremely low resolution. In addition, optical axis differences cause an additional image mosaic issue.

Benefiting from the development of computational imaging techniques, high-resolution images can now be obtained using a single photodetector (PD).[12,13] In recent years, researchers have conducted a series of studies focusing on different aspects of computational imaging, including imaging methods, projection equipment, spectrum extension, and applications.[14–24] In particular, we developed perovskite cameras that can realize 256×256 pixel imaging;[25] therefore, we can use the proposed PDs to realize functional imaging.[26–29] Herein, we replaced numerous ommatidia with a single convex PD coupled with an imaging algorithm to realize the function of the compound eye. We also incorporated perovskite materials in this study because of their high optoelectronic performance and simple fabrication process.[22–24,30,31] Therefore, the perovskite materials can be widely applied in photoelectric devices, like solar cells,[32–34] LEDs,[35–39] and PDs.[40–43] In addition, the perovskite photosensitive materials can be spin-coated onto a flexible substrate to form a large-area flexible perovskite PD (FP-PD) to collect light from a wide-angle range,[44–46] enabling one to deform the camera into any desired shape. We set up a prototype FP-PD camera by combining a large-area FP-PD with the corresponding imaging algorithm, as shown in Figure 1c. In the FP-PD camera, the four-step phase-shifting sinusoidal patterns projected by a projector can be regarded as a light source; the convex FP-PD is a photosensitive element, similar to a retina or CCD, and the spatial reflectivity of the imaging scene can be restored through inverse Fourier transformation. The FP-PD used requires a large area to be bent at a large angle, which gives the FP-PD camera a wide FOV, as depicted in the inset of Figure 1c. Detailed descriptions of the FP-PD camera prototype, including the setup and imaging algorithm, are provided in Section S1, Supporting Information (Figures S1–S3, Supporting Information). Based on the above discussion, the proposed FP-PD camera simultaneously exhibits the advantages of wide-angle FOV, high resolution, and low image distortion, whereas the existing fisheye and compound eye cameras cannot meet all the three merits, as shown in Figure 1d. Therefore, the proposed FP-PD camera is a new-generation wide-FOV camera that outperforms the other two.

2. Results and Discussion

2.1. Performance Characterization of the Large Area FP-PD

The lightweight and bendable flexible PDs are easier to be adapted to the complicated application environment than rigid PDs.[47,48] Recently, solution-processed and cost-effective organic–inorganic hybrid perovskites have been applied in flexible optoelectronics.[49–51] Most researchers focused on the integration and miniaturization of flexible PDs, such as micro–nano PDs, which are able to maintain their excellent performance when bent; however, they lose the ability to receive wide-angle optical signals, as shown in the insets of Figure 1c. Therefore, to obtain the capability of wide-angle optical signals, we designed a large-area FP-PD with an active area (0.14 cm^2) and length in square centimeters, as shown in **Figure 2**a. The FP-PD fabrication process is shown in Figure S4, Supporting Information. The FP-PD has a $SnO_2/TiO_2/MAPbI_3$/Spiro-OMeTAD structure and the flexible substrate is PEN/ITO. The FP-PD is fabricated through a solution method and improved by atomic layer deposition (ALD).[29,52] The details of the fabrication method, material characterization, and FP-PD are shown in Figure S5, Supporting Information. As shown in Figure 2b, the uniform and compact ALD-TiO_2 layer can effectively reduce the dark current by three orders of magnitude compared to the FP-PD and increase the ON/OFF ratio to 3300 from 10. Figure 2c shows the noise spectral density of the FP-PDs with and without the TiO_2 layer through Fourier transformation from the time-domain dark-current waveform (insets of Figure 2c).[53] We can observe that the introduction of TiO_2 can suppress the noise power by three to four orders of magnitude. Benefiting from noise current suppression, the optimized FP-PD exhibited excellent faint light detection with a detectable light intensity limit of 35 nW cm^{-2}. Furthermore, we measured the photoresponse characteristics of the FP-PD with and without the TiO_2 layer under irradiation with different light intensities using a 660 nm laser. Figure 2d shows a broad linear dynamic range (LDR) at 0 V bias, which is commonly expressed on a logarithmic scale; LDR = $20\log(P_{max}/P_{min})$, where P_{max} and P_{min} denote the upper and lower limits of light intensity in the linear region, respectively. The optimized FP-PD exhibits a linear response from 35 nW cm^{-2} to 0.7 W cm^{-2}, corresponding to LDR of 126 dB, which is significantly better than 72 dB that of the FP-PD without the TiO_2 layer. The LDR of the proposed FP-PDs should be larger than the obtained values because the maximum light intensity of the 660 nm laser in our laboratory was limited to 0.7 W cm^{-2}. Because the structure of the proposed FP-PD is a type of vertical photovoltaic device, the proposed FP-PD inherits the self-powered (or self-driven) characteristics of photovoltaic devices. Figure 2e illustrates the semi-log I–V curves under dark and light conditions, demonstrating the self-powered capability of the optimized FP-PD. The optimized FP-PD exhibited a large ON/OFF ratio of 386 at an external bias of 0 V (660 nm, 1 μW cm^{-2}).

Responsivity (R) is a key figure of merit expressed as $R = I_{ph}/(P_A)$, where I_{ph} denotes the photocurrent, P is the irradiated light intensity, and A is the active area of the PD. The photocurrent and R plots at various voltages are shown in Figure 2f. It can be observed that R increases from 0.025 to 1.6 A W^{-1} with an increase in the reverse bias from 0 to –1 V. Figure 2g depicts the wavelength-dependent R of the optimized FP-PD under a 0 V bias, whereas the wavelength-dependent irradiated light intensities are shown in Figure S6, Supporting Information. It is observed that the FP-PD can detect full visible wavelength from 300 to 800 nm.

Detectivity (D^*) is an important parameter for evaluating the weak light-detection ability of PDs. However, although

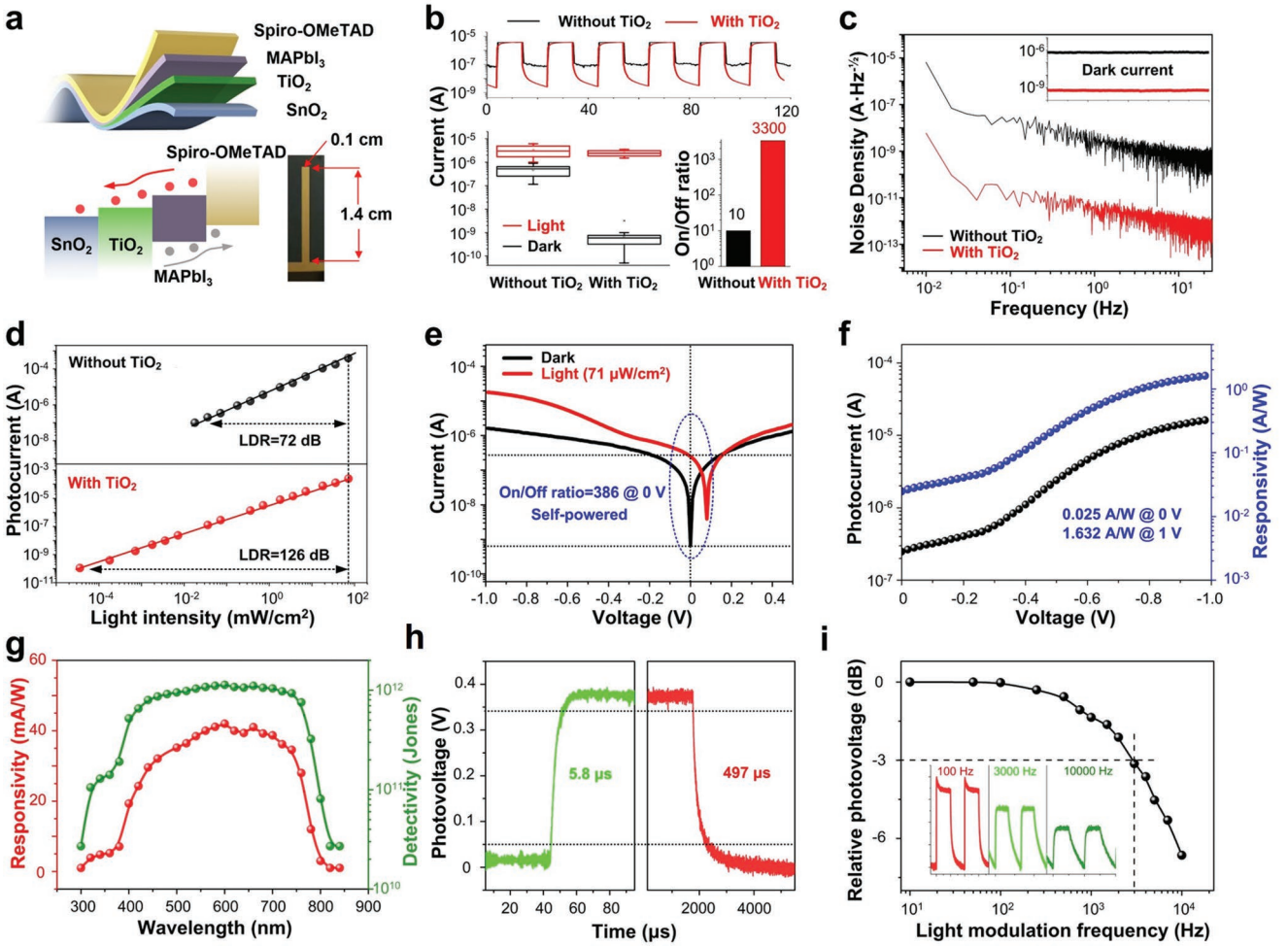

Figure 2. Performance characterization of the large area FP-PD. a) Structure, band energy, and photograph of the FP-PD. The active area is 14 mm × 1 mm. b) Performance optimization of the FP-PD by introducing the ALD-TiO_2 layer between SnO_2 and perovskite, including the *I–T* curve, statistics of dark current and light current, and ON/OFF ratio of the FP-PD with and without the ALD-TiO_2 layer (660 nm, 0.714 mW cm^{-2}). c) Analysis of noise spectral density of the FP-PD with and without the ALD-TiO_2 layer based on the dark current waveform in the inset. d) Photocurrent of the FP-PD with and without the ALD-TiO_2 layer versus different incident light intensities at 0 V bias. e) Semi-log *I–V* curves of the optimized FP-PD in light and dark conditions. f) Bias-dependent photocurrent and responsivity of the optimized FP-PD. g) Wavelength-dependent responsivity and detectivity curves of the optimized FP-PD. h) Time-dependent photovoltage curve of the optimized FP-PD to measure response speed. i) Frequency response of the optimized FP-PD. Insets: the temporal photovoltage response at 100, 3000, and 10 000 Hz.

Huang et al. proposed some guidelines for the accurate characterization of PDs,[54] confusing and inconsistent calculation methods for D^* significantly affect the evaluation of PDs in different reports. For a better comparison with other flexible PDs, we adopted a simplified expression to determine D^*; $D^* = RA^{0.5}/(2qI_{dark})^{0.5}$, where R denotes the responsivity, I_{dark} is the dark current, q is the elementary charge, and A is the active area of the PD. The simplified D^* calculation simply considers the shot noise of the dark current; however, it ignores the low-frequency noise (1/*f* noise) and light current shot noise and tends to overestimate the D^* of PDs. According to the simplified expression, the wavelength-dependent D^* under a 0 V bias is shown in Figure 2g. It indicates that the D^* of the optimized FP-PD can be estimated to be greater than 1×10^{12} cm $Hz^{1/2}$ W^{-1} (Jones), which is comparable to values reported in previous studies. To better uncover the ability of the FP-PDs to detect weak light, the D^* values were determined using the noise equivalent power (NEP) and noise power spectra (Figure 2c), where $D^* = (AB)^{0.5}/\text{NEP} = R(AB)^{0.5}/i_n$, where A denotes the active area of the device and B is the electrical bandwidth, as shown in Figure S6, Supporting Information.

The response speed (including rise time and decay time) is also a key parameter of PDs, where the rise time is generally defined as the time required for the photocurrent to increase from 10% to 90% and the inverse of the decay time. As shown in Figure 2h, the optimized FP-PD exhibits the response speed with the increase and decrease of photovoltage as 5.8 and 497 μs, respectively. Figure 2i illustrates the plot of the frequency response of the FP-PD, exhibiting a −3 dB cutoff frequency close to 3000 Hz. The insets of Figure 2i indicate that the FP-PD retains an excellent response waveform at a high modulation frequency of 10 000 Hz. Table S1, Supporting Information, lists the performance comparison of flexible $MAPbI_3$ perovskite PDs reported in previous studies. This demonstrates that the

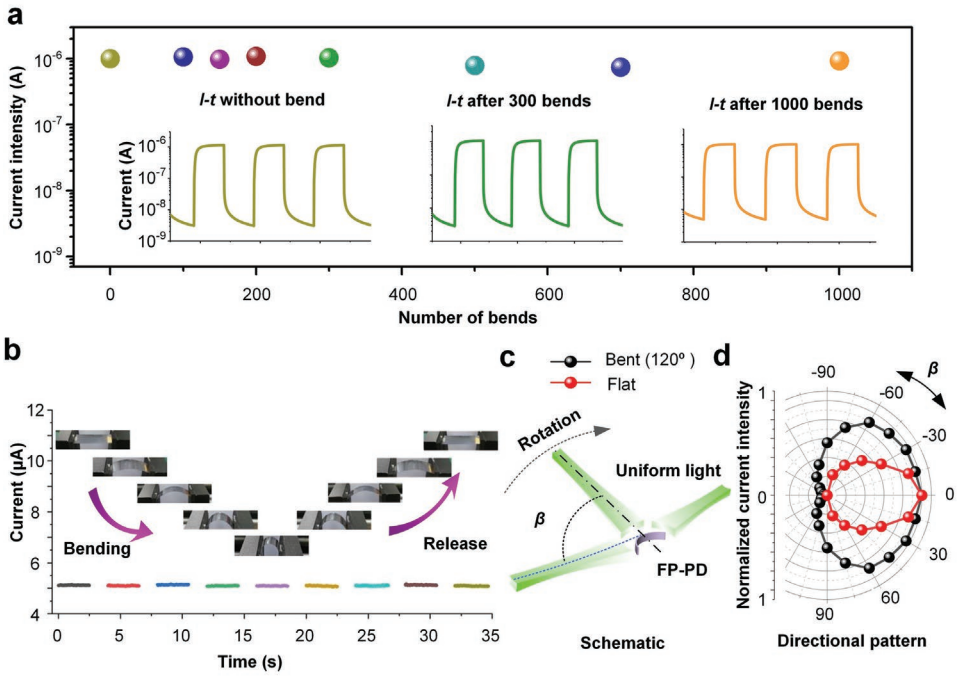

Figure 3. Bending performance of the FP-PD. a) Plot of light current versus bending cycle number under 660 nm with 0.1 mW. Insets: ON/OFF switching behaviors after 0, 300, and 1000 bending cycles. b) Time-domain light current when the FP-PD is being bent and released. Insets: corresponding photographs of the FP-PD. Here, the focused laser is always vertically irradiating to the center of the FP-PD whether it bends or not. c) Schematic of FOV measurement irradiated by a large-area uniform light. d) Directional pattern of the FP-PD suggesting that the PD at bent status ($\alpha_{PD} \approx 120°$) has a larger FOV (α_F) than that at flat state.

proposed device is highly competitive in terms of responsivity, detectivity, LDR, and response time, in addition to possessing unique large-area characteristics, which favor wide FOV performance.

2.2. Bending Performance of the FP-PD

Figure 3 focuses on the bending performance of the FP-PD, which directly determines the quality of wide-angle FOV imaging of the FP-PD. First, we tested the photoresponse uniformity at different points of the FP-PD by raster scanning of the focused laser illustrated in Figure S7, Supporting Information. The photoresponse uniformity ensured that light was received from different directions by the FP-PD after bending. The current mapping in Figure S7, Supporting Information, at different light intensities indicates that the proposed FP-PD possesses excellent photoresponse uniformity, which remains unchanged under bending. Moreover, we performed repeated bending/straitening test over 1000 times, as shown in Figure 3a. In addition, Figure 3b shows the time-domain light current curve (*I*–*t*) of the FP-PD during the process of bending and releasing. In the process, the focused laser maintained the same power (600 nm, 0.1 mW) and always vertically irradiated the center of the FP-PD, ensuring the accuracy of the measurement results. These results demonstrate that FP-PD exhibited excellent mechanical flexibility and durability.

The FOV can be measured by irradiating large-area uniform white light, which is similar to the light source in practical imaging, as shown in Figure 3c. The measurement results demonstrate that the PD in the bent state ($\alpha_{PD} \approx 120°$) has a larger FOV (α_F) than that in the flat state, as shown in Figure 3d. Here, β is the directional angle, which is the angle between the object (or light) and normal. In particular, the results indicate that PD in the bent state has the ability to perceive light more than 90° ($\alpha_F > 180°$). The FOV increased because lights at different angles could find their nearly parallel optical axis because each region of the FP-PD had its own optical axis, similar to the insect compound eye. Therefore, the FP-PD camera is expected to have a wide-angle FOV ($\alpha_F > 180°$).

2.3. Imaging FOV and Low-Distortion Performance of the FP-PD Camera

Figure 4 demonstrates the wide-angle FOV and distortion-free characteristics of the FP-PD camera from the perspective of imaging performance. Some supplemental data from the imaging experiments can be found in Section S3, Supporting Information (Figure S8, Supporting Information).[18,19] In a real-world scenario, the direction of the projection light usually remains the same, as shown in Figure 4a. In this case, the reflection efficiencies of different regions in the image scene are different, that is, the reflected light of the region facing the main optical axis has a larger number of photons arriving at the FP-PD. Therefore, the measured FOV of the camera is expected to be slightly smaller than that of the FP-PD as shown in Figure 3d, and this has been proven experimentally,

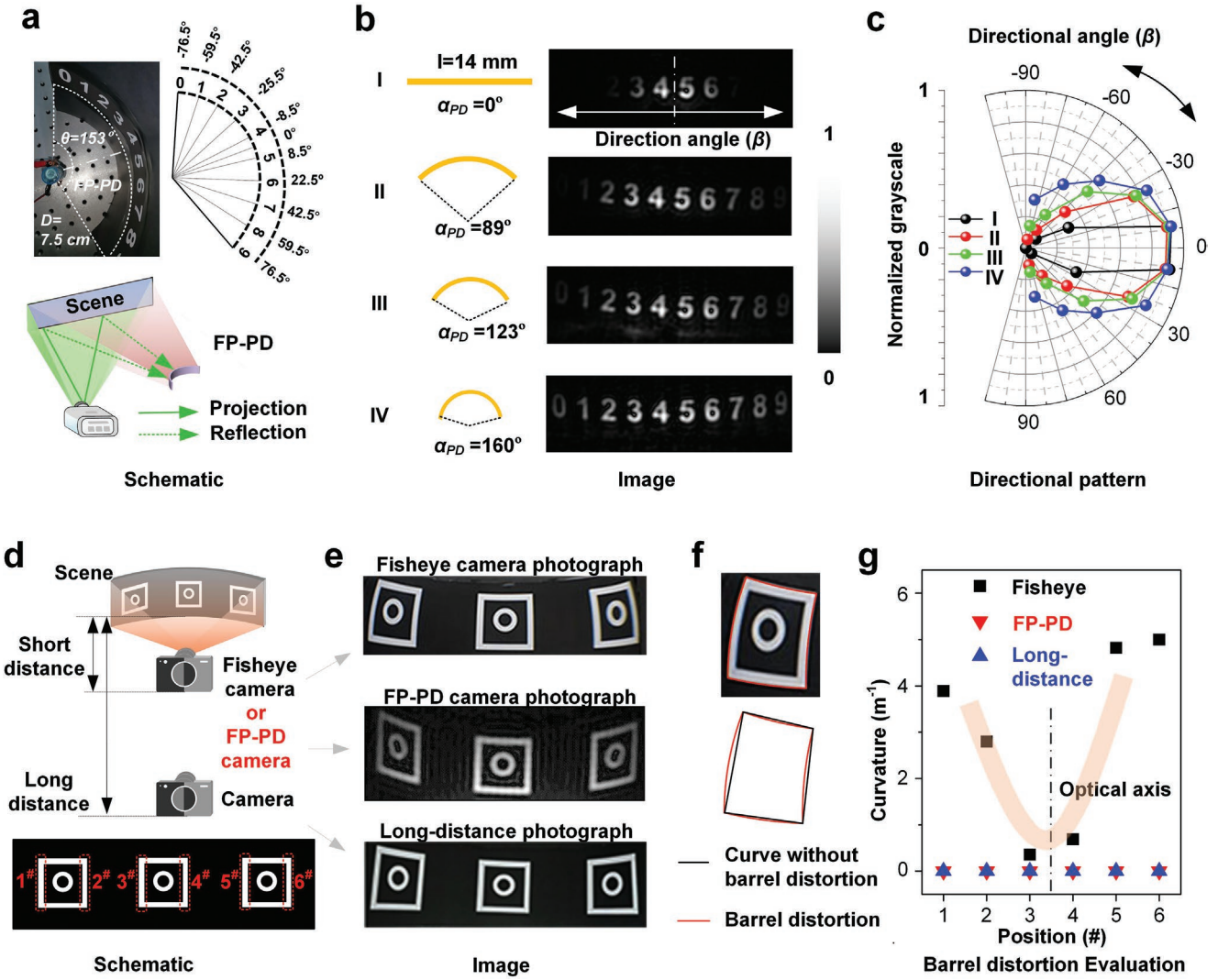

Figure 4. FOV performance and distortion-free of the FP-PD camera. a) Schematic of imaging experiments when the scene is in a different directional angle (β). b) Imaging results in conditions with different bending angles (α_{PD}). c) Directional pattern obtained from images in (b), suggesting that the PD with a larger bending angle (α_{PD}) has a larger FOV (α_F). d) Schematic of imaging experiments to demonstrate the barrel distortion problem. e) Imaging results and fisheye camera images in the conditions descripted in (d). f) A typical barrel distortion curve (red) extracted from the image in (g), compared with expected non-barrel distortion curve (black). g) Calculated curvature of barrel distortion in fisheye camera image and the FP-PD camera image.

as shown in Figure 4b,c. The FP-PD camera can still see the object inside the view, although it is darker than that in the front view. These experimental results also demonstrate that the larger the bending angle (α_{PD}) of the FP-PD, the wider the FOV (α_F). The FOV depends on whether the diffused light from the imaging target can be received by the PD; therefore, the intensity of the received light depends on the intensity of the illumination light, reflectivity of the imaging target, reflection angle, and the receiving efficiency of the PD (including responsibility and angle dependence characteristics). Figure 3d illustrates the FOV shown in Figure 3c (PD receiving efficiency) without considering the intensity of the illumination light, reflectivity of the imaging target, and reflection angle. However, in reality, the reflection angle must be considered, as shown in Figure 4a, and the FOV in this situation (Figure 4c) is usually slightly less than the FOV obtained without considering the reflection angle, as shown in Figure 3d. Figure 3d illustrates the FOV of the FP-PD, whereas Figure 4c illustrates the FOV of the imaging system. In brief, the FP-PD camera exhibits excellent FOV-tunable capability.

As mentioned in the introduction, fisheye cameras can achieve a wide-angle FOV; however, they suffer from barrel distortion. Figure 4d illustrates a schematic to experimentally demonstrate the barrel distortion problem. The commercial fisheye and FP-PD cameras were placed at the same position, which was very close to the scene (≈10 cm). Figure 4e presents the imaging results under similar conditions, from which we can clearly observe barrel distortion, while long-distance (≈1 m) photograph has no obvious barrel distortion. Figure S9, Supporting Information, illustrates significantly distorted images captured using fisheye cameras. Figure 4f shows a typical barrel distortion curve (red) extracted from the fisheye camera image

compared with the expected non-barrel distortion curve (black). To quantitatively evaluate barrel distortion, we determined the curvatures of barrel distortion in fisheye and FP-PD camera images, as shown in Figure 4g. From these results, we can conclude that the FP-PD camera has hardly any barrel distortion.

2.4. High-Resolution Imaging Results

To image real scenes, the first step is to improve resolution. A 2D image can be converted into the frequency domain through Fourier transformation; low frequencies determine the outline, whereas high frequencies determine the details. We set the spectrum coverage (S) of the original photograph at 100%. **Figure 5**a illustrates the spectra after low-pass filtering when the cut-off frequency decreased, that is, when S decreased. Note that a spectrum coefficient has a real part and an imaginary part; here, we demonstrate the modulus of the complex coefficients. Figure 5b illustrates filtered images corresponding to filtered spectra in Figure 5a. Therefore, theoretical analysis and simulation experiments demonstrated that it is necessary to obtain as much high-frequency information as possible to improve resolution.

To lossless reconstruct an image resolution with $I \times J$ pixels, all the Fourier spectrum coefficients ($I \times J$) must be obtained. Because each Fourier coefficient requires the projection of a Fourier base pattern with a four-step phase shift, it requires four measurements. In addition, because the image is a real-valued matrix mathematically, its Fourier spectra be conjugate symmetric; therefore, full sampling of the image requires $m = 2 \times I \times J$ measurements. In this experiment, full sampling of the 256 × 256 image required m = 131072 measurements. Figure 5c illustrates the experimentally obtained spectra when the measurement number (m) increased, whereas Figure 5d

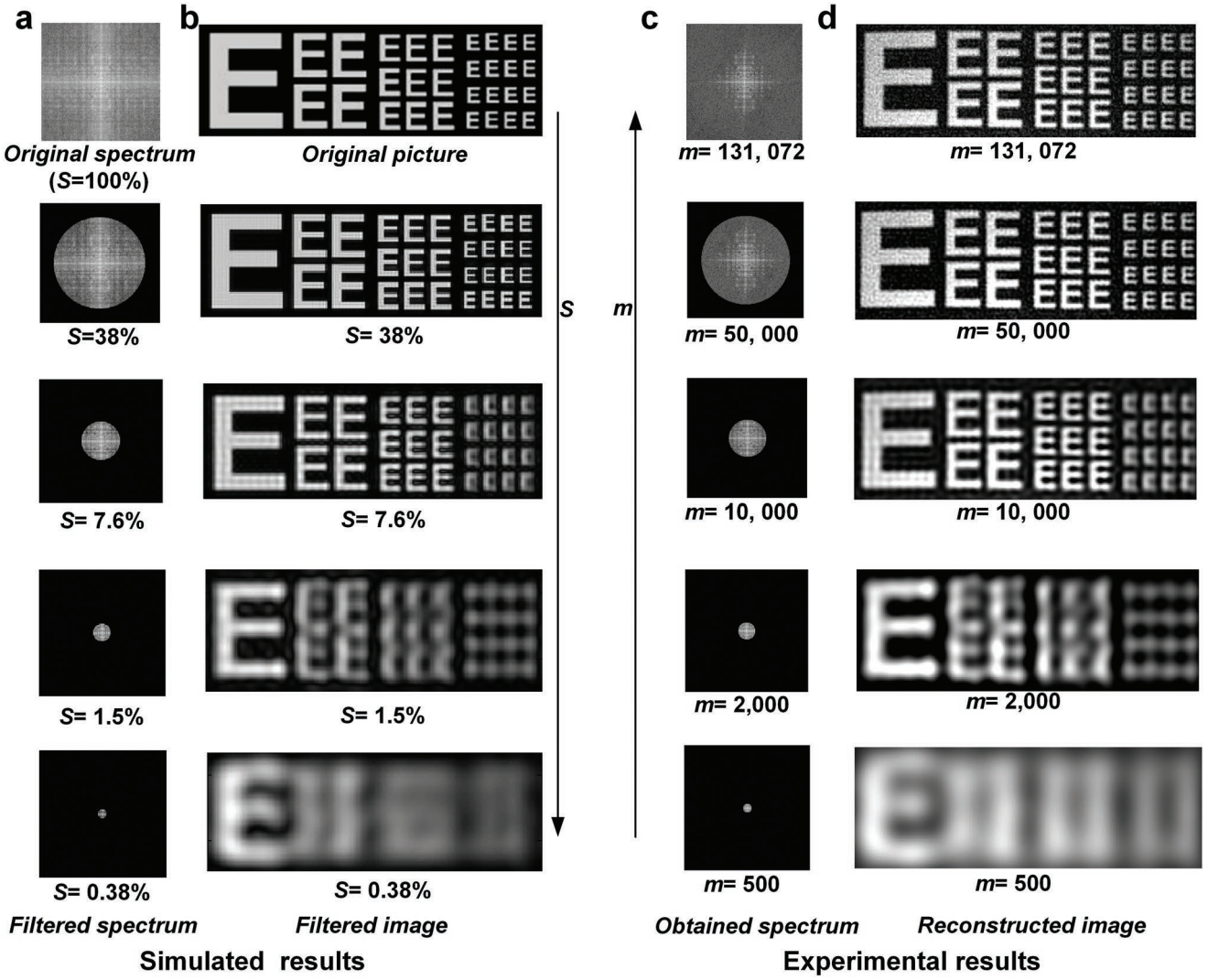

Figure 5. High-resolution imaging results. a) Spatial spectra after low pass filtering when the cut-off frequency decreases (from the top down). Top is the original spectrum. b) The filtered images corresponding to the spectra in (a). Top is the original 256 × 256 photograph (only ≈84 × 256 displayed) taken using a commercial camera. Note that the photograph is taken from a long distance. c) Obtained spectra when measurement number (m) increases (from the bottom up). d) Reconstructed images through inverse Fourier transformation corresponding to the images in (c). Note that the image by the FP-PD camera is taken from a short distance.

illustrates the reconstructed images through inverse Fourier transformation corresponding to those illustrated in Figure 5c. Here, m = 50 000 and S = 38% are equivalent. Considering the obtained results, we can conclude that the simulation and experimental results are consistent. Note that 256 × 256 pixels are not the limitation of the FP-PD camera because we can increase the higher frequency component of the projection light and the number of measurements (m).

Because FP-PD has a wide-angle spectral response covering the visible light range, the FP-PD camera can take color photographs. Figure S10, Supporting Information, shows the red channel (R), green channel (G), blue channel (B), and composited RGB images obtained using the trichromatic method. Both the shape and color of the RGB image are in accordance with those in conventional camera photographs, indicating that the proposed FP-PD camera has a color imaging capability. In addition, the proposed FP-PD camera exhibits several fascinating merits. For instance, clear images can be obtained even when a high-scattering medium, such as frosted glass, is placed in front of the camera. As illustrated in Figure S10b, Supporting Information, a piece of frosted glass is placed in front of the FP-PD. If it is a conventional camera with a frosted glass covering, the photograph cannot be seen clearly. However, the FP-PD camera images with and without frosted glass are almost identical, as shown in Figure S10c, Supporting Information. This can be attributed to the fact that frosted glass can be regarded as an attenuator, which can cause a lower signal-to-noise ratio (decreased by ≈23%), as shown in Figure S10d, Supporting Information, but not at a lower resolution.

The FOV and resolution performances of the camera have been discussed in Figures 4 and 5, respectively. How the other photoelectric properties of the FP-PD contribute to the camera performance? it can be divided into three categories. First, some camera performances basically depend on the properties of the FP-PD, like LDR, weak-light performance, and spectral response. Thereinto, a good weak-light performance requires high responsivity and low current fluctuation that has been discussed in our previous work.[25] Second, some camera performances are partially affected by the FP-PD, like imaging speed and white balance. Thereinto, imaging speed depends on response speed of the FP-PD and pattern projection speed simultaneously, and the details can be seen in the Supporting Information. Finally, some camera performances are basically independent of detector parameters, like depth of field and focal length, which depends on projection lens.

3. Conclusion

In this paper, we present materials, mechanisms, and integration schemes that afford scalable pathways to an FP-PD camera to achieve a remarkable FOV greater than 150° and better than that of the human eye. The experimental results demonstrated that the proposed FP-PD camera has exciting advantages of simultaneously achieving a tunable wide-angle FOV, low image distortion, and high resolution, whereas existing fisheye and compound eye cameras do not simultaneously satisfy all the three requirements. Therefore, we expect this FP-PD camera to be a novel wide-FOV camera with several interesting applications.

4. Experimental Section

The fabrication process of the FP-PD is shown in Figure S4a, Supporting Information, including steps 1–7. First (step 1,2), the SnO_2 layer was spin-coated onto the flexible PEN (Polyethylene naphthalate two formic acid glycol ester) substrate (treated by UV–ozone cleaner for 15 min before use) at 4000 rpm for 30 s, and then annealed at 150 °C for 30 min. The SnO_2 aqueous solution was supplied by Xi'an Polymer Light Technology Corp, and PEN/ITO substrates were supplied by Advanced Election Technology Co., Ltd. Here PEN (rather than polyethylene terephthalate [PET]) was used as flexible substrate due to that PEN had better heat resistance than PET, which allowed PEN to adapt the high temperature of steps 2 and 3 of fabrication process. Second (step 3), before preparation of methylammonium lead tri-iodide ($MAPbI_3$) perovskite, an ultra-thin TiO_2 film (10 nm) was deposited on the PEN/ITO/SnO_2 to improve the performance of FP-PD according to previous works.

Next (step 4, 5), the $MAPbI_3$ perovskite film was spin-coated on the PEN/ITO/SnO_2/ALD-TiO_2 by one-step method. The $MAPbI_3$ precursor solution consisted of PbI_2 (461 mg), MAI (159 mg), and dimethyl sulfoxide (1 mL). The perovskite film was obtained by spin-coating at 4000 rpm for 30 s, then heated for 15 min at 100 °C in a glove box (step 6). Above materials were purchased from Advanced Election Technology Co., Ltd. Finally (step 7), an Au electrode was deposited on the top of $MAPbI_3$ perovskite film by a mask. Figure S4a[7,8], Supporting Information, shows the diagrams of the FP-PD device before and after cutting. The photographs of the FP-PD are shown in Figure S4b,c, Supporting Information. The fabricated $MAPbI_3$ perovskite on the PEN/AP substrate was characterized by SEM, absorption spectra, and X-ray diffraction as shown in Figure S7b–d, Supporting Information. These results were consistence with previous reported.

Supporting Information

Supporting Information is available from the Wiley Online Library or from the author.

Acknowledgements

Z.J. and Y.L. contributed equally to this work. The authors thank Hengchao Sun, Haibao Wang, Prof. Zibang Zhang, and Prof. Jingang Zhong for experiment setup and helpful discussions. The authors acknowledge the financial supports from the National Natural Science Foundation of China (Nos. 51772135, 52172202, and 62105123).

Conflict of Interest

The authors declare no conflict of interest.

Data Availability Statement

Research data are not shared.

Keywords

imaging, perovskites, photodetectors, wide field-of-view cameras

Received: July 31, 2022
Revised: August 26, 2022
Published online: September 7, 2022

[1] P. Artal, A. Benito, J. Tabernero, *J. Vision* **2006**, *6*, 1.
[2] I. Jung, J. Xiao, V. Malyarchuk, C. Lu, M. Li, Z. Liu, J. Yoon, Y. Huang, J. A. Rogers, *Proc. Natl. Acad. Sci. U. S. A.* **2011**, *108*, 1788.
[3] K. Zhang, Y. H. Jung, S. Mikael, J.-H. Seo, M. Kim, H. Mi, H. Zhou, Z. Xia, W. Zhou, S. Gong, Z. Ma, *Nat. Commun.* **2017**, *8*, 1782.
[4] L. Gu, S. Poddar, Y. Lin, Z. Long, D. Zhang, Q. Zhang, L. Shu, X. Qiu, M. Kam, A. Javey, Z. Fan, *Nature* **2020**, *581*, 278.
[5] H. Fu, L. Bian, X. Cao, J. Zhang, *Opt. Express* **2020**, *28*, 314.
[6] M. S. Kim, G. J. Lee, C. Choi, M. S. Kim, M. Lee, S. Liu, K. W. Cho, H. M. Kim, H. Cho, M. K. Choi, N. Lu, Y. M. Song, D.-H. Kim, *Nat. Electron.* **2020**, *3*, 546.
[7] L. C. Kogos, Y. Li, J. Liu, Y. Li, L. Tian, R. Paiella, *Nat. Commun.* **2020**, *11*, 1637.
[8] K.-H. Jeong, J. Kim, L. P. Lee, *Science* **2016**, *312*, 557.
[9] D. Floreano, R. Pericet-Camara, S. Viollet, F. Ruffier, A. Brückner, R. Leitel, W. Buss, M. Menouni, F. Expert, R. Juston, M. K. Dobrzynski, G. L'Eplattenier, F. Recktenwalde, H. A. Mallote, N. Franceschini, *Proc. Natl. Acad. Sci. U. S. A.* **2013**, *110*, 9267.
[10] L. Zhu, Y. L. Zhang, H. B. Sun, *Light: Adv. Manuf.* **2021**, *2*, 284.
[11] Y. M. Song, Y. Xie, V. Malyarchuk, J. Xiao, I. Jung, K.-J. Choi, Z. Liu, H. Park, C. Lu, R.-H. Kim, R. Li, K. B. Crozier, Y. Huang, J. A. Rogers, *Nature* **2013**, *497*, 95.
[12] M. P. Edgar, G. M. Gibson, M. J. Padgett, *Nat. Photonics* **2019**, *13*, 13.
[13] G. M. Gibson, S. D. Johnson, M. J. Padgett, *Opt. Express* **2020**, *28*, 28190.
[14] Z. Zhang, X. Ma, J. Zhong, *Nat. Commun.* **2015**, *6*, 6225.
[15] M.-J. Sun, M. P. Edgar, G. M. Gibson, B. Sun, N. Radwell, R. Lamb, M. J. Padgett, *Nat. Commun.* **2016**, *7*, 12010.
[16] C. M. Watts, D. Shrekenhamer, J. Montoya, G. Lipworth, J. Hunt, T. Sleasman, S. Krishna, D. R. Smith, W. J. Padilla, *Nat. Photonics* **2014**, *8*, 605.
[17] J. Yang, L. Gong, X. Xu, P. Hai, Y. Shen, Y. Suzuki, L. V. Wang, *Nat. Commun.* **2017**, *8*, 780.
[18] M. P. Edgar, G. M. Gibson, M. J. Padgett, *Nat. Photonics* **2019**, *13*, 13.
[19] B. Sun, M. P. Edgar, R. Bowman, L. E. Vittert, S. Welsh, A. Bowman, M. J. Padgett, *Science* **2013**, *340*, 844.
[20] S. Ota1, R. Horisaki, Y. Kawamura1, M. Ugawa1, I. Sato, K. Hashimoto, R. Kamesawa, K. Setoyama, S. Yamaguchi, K. Fujiu, K. Waki, H. Noji, *Science* **2018**, *360*, 1246.
[21] D. B. Phillips, M.-J. Sun, J. M. Taylor, M. P. Edgar, S. M. Barnett, G. M. Gibson, M. J. Padgett, *Sci. Adv.* **2017**, *3*, e1601782.
[22] C. Bao, W. Xu, J. Yang, S. Bai, P. Teng, Y. Yang, J. Wang, N. Zhao, W. Zhang, W. Huang, F. Gao, *Nat. Electron.* **2020**, *3*, 156.
[23] J. Feng, C. Gong, H. Gao, W. Wen, Y. Gong, X. Jiang, B. Zhang, Y. Wu, Y. Wu, H. Fu, L. Jiang, X. Zhang, *Nat. Electron.* **2018**, *1*, 404.
[24] Y. Chen, Y. Lei, Y. Li, Y. Yu, J. Cai, M.-H. Chiu, R. Rao, Y. Gu, C. Wang, W. Choi, H. Hu, C. Wang, Y. Li, J. Song, J. Zhang, B. Qi, M. Lin, Z. Zhang, A. E. Islam, B. Maruyama, S. Dayeh, L.-J. Li, K. Yang, Y.-H. Lo, S. Xu, *Nature* **2020**, *577*, 209.
[25] Z. Ji, Y. Liu, M. Yao, Z. Zhang, J. Zhong, W. Mai, *Adv. Funct. Mater.* **2021**, *31*, 2104320.
[26] Y. Liu, C. Liu, K. Shen, P. Sun, W. Li, C. Zhao, Z. Ji, Y. Mai, W. Mai, *ACS Nano* **2022**, *16*, 5820.
[27] Q. Wu, Y. Liu, X. Huang, X. Zheng, J. He, Z. Ji, W. Mai, *Sci. China: Technol. Sci.* **2021**, *64*, 2523.
[28] Y. Liu, Z. Ji, Y. Li, H. Fan, W. Mai, *Photonics Res.* **2021**, *9*, 1734.
[29] Z. Ji, Y. Liu, W. Mai, *Opt. Lett.* **2021**, *46*, 150.
[30] J. Li, L. Xu, T. Wang, J. Song, J. Xue, Y. Dong, B. Cai, X. Li, H. Zeng, *Adv. Mater.* **2017**, *29*, 1603885.
[31] J. Song, J. Li, X. Li, L. Xu, Y. Dong, H. Zeng, *Adv. Mater.* **2015**, *27*, 7162.
[32] H. Min, D. Y. Lee, J. Kim, G. Kim, K. S. Lee, J. Kim, M. J. Paik, Y. K. Kim, K. S. Kim, M. G. Kim, T. J. Shin, S. I. Seok, *Nature* **2021**, *598*, 444.
[33] J. J. Yoo, G. Seo, M. R. Chua, T. G. Park, Y. Lu, F. Rotermund, Y.-K. Kim, C. S. Moon, N. J. Jeon, J.-P. Correa-Baena, V. Bulović, S. S. Shin, M. G. Bawendi, J. Seo, *Nature* **2021**, *590*, 587.
[34] T. Wu, Z. Qin, Y. Wang, Y. Wu, W. Chen, S. Zhang, M. Cai, S. Dai, J. Zhang, J. Liu, Z. Zhou, X. Liu, H. Segawa, H. Tan, Q. Tang, J. Fang, Y. Li, L. Ding, Z. Ning, Y. Qi, Y. Zhang, L. Han, *Nano-Micro Lett.* **2021**, *13*, 152.
[35] J. Chen, J. Wang, X. Xu, J. Li, J. Song, S. Lan, S. Liu, B. Cai, B. Han, J. T. Precht, D. Ginger, H. Zeng, *Nat. Photonics* **2021**, *15*, 238.
[36] R. Wang, H. Xiang, J. Chen, Y. Li, Y. Zhou, W. C. H. Choy, Z. Fan, H. Zeng, *ACS Energy Lett.* **2022**, *7*, 2173.
[37] Y. Zhou, T. Fang, G. Liu, H. Xiang, L. Yang, Y. Li, R. Wang, D. Yan, Y. Dong, B. Cai, H. Zeng, *Adv. Funct. Mater.* **2021**, *31*, 2106871.
[38] H. Xiang, R. Wang, J. Chen, F. Li, H. Zeng, *Light: Sci. Appl.* **2021**, *10*, 206.
[39] J. Luo, X. Wang, S. Li, J. Liu, Y. Guo, G. Niu, L. Yao, Y. Fu, L. Gao, Q. Dong, C. Zhao, M. Leng, F. Ma, W. Liang, L. Wang, S. Jin, J. Han, L. Zhang, J. Etheridge, J. Wang, Y. Yan, E. H. Sargent, J. Tang, *Nature* **2018**, *563*, 541.
[40] F. Wang, X. Zou, M. Xu, H. Wang, H. Wang, H. Guo, J. Guo, P. Wang, M. Peng, Z. Wang, Y. Wang, J. Miao, F. Chen, J. Wang, X. Chen, A. Pan, C. Shan, L. Liao, W. Hu, *Adv. Sci.* **2021**, *8*, 2100569.
[41] H.-P. Wang, S. Li, X. Liu, Z. Shi, X. Fang, J.-H. He, *Adv. Mater.* **2021**, *33*, 2003309.
[42] Z. Han, W. Fu, Y. Zou, Y. Gu, J. Liu, B. Huang, D. Yu, F. Cao, X. Li, X. Xu, H. Zeng, *Adv. Mater.* **2021**, *33*, 2003852.
[43] J. Wang, Y. Zhang, J. Chen, Y. Wei, D. Yu, L. Liang, Y. Liu, Y. Wu, W. Shen, X. Li, H. Zeng, *ACS Appl. Mater. Interfaces* **2021**, *13*, 36147.
[44] Y. Lei, Y. Chen, R. Zhang, Y. Li, Q. Yan, S. Lee, Y. Yu, H. Tsai, W. Choi, K. Wang, Y. Luo, Y. Gu, X. Zheng, C. Wang, C. Wang, H. Hu, Y. Li, B. Qi, M. Lin, Z. Zhang, S. A. Dayeh, M. Pharr, D. P. Fenning, Y.-H. Lo, J. Luo, K. Yang, J. Yoo, W. Nie, S. Xu, *Nature* **2020**, *583*, 790.
[45] T. Bu, J. Li, F. Zheng, W. Chen, X. Wen, Z. Ku, Y. Peng, J. Zhong, Y.-B. Cheng, F. Huang, *Nat. Commun.* **2018**, *9*, 4609.
[46] Y. Liu, Y. Zhang, Z. Yang, H. Ye, J. Feng, Z. Xu, X. Zhang, R. Munir, J. Liu, P. Zuo, Q. Li, M. Hu, L. Meng, K. Wang, D.-M. Smilgies, G. Zhao, H. Xu, Z. Yang, A. Amassian, J. Li, K. Zhao, S. (F.) Liu, *Nat. Commun.* **2018**, *9*, 5302.
[47] C. Fuentes-Hernandez, W.-F. Chou, T. M. Khan, L. Diniz, J. Lukens, F. A. Larrain, V. A. Rodriguez-Toro, B. Kippelen, *Science* **2020**, *370*, 698.
[48] J. Zhao, L. Zhao, Y. Deng, X. Xiao, Z. Ni, S. Xu, J. Huang, *Nat. Photonics* **2020**, *14*, 612.
[49] D. Hao, J. Zou, J. Huang, *InfoMat* **2020**, *2*, 139.
[50] W. Hu, W. Huang, S. Yang, X. Wang, Z. Jiang, X. Zhu, H. Zhou, H. Liu, Q. Zhang, X. Zhuang, J. Yang, D. H. Kim, A. Pan, *Adv. Mater.* **2017**, *29*, 1703256.
[51] G. Cen, Y. Liu, C. Zhao, G. Wang, Y. Fu, G. Yan, Y. Yuan, C. Su, Z. Zhao, W. Mai, *Small* **2019**, *15*, 1902135.
[52] Z. Ji, Y. Liu, W. Li, C. Zhao, W. Mai, *Sci. Bull.* **2020**, *65*, 1371.
[53] C.-H. Liu, Y.-C. Chang, T. B. Norris, Z. Zhong, *Nat. Nanotechnol.* **2014**, *9*, 273.
[54] Y. Fang, A. Armin, P. Meredith, J. Huang, *Nat. Photonics* **2019**, *13*, 1.